

Dalton Transactions

Accepted Manuscript



This is an *Accepted Manuscript*, which has been through the Royal Society of Chemistry peer review process and has been accepted for publication.

Accepted Manuscripts are published online shortly after acceptance, before technical editing, formatting and proof reading. Using this free service, authors can make their results available to the community, in citable form, before we publish the edited article. We will replace this *Accepted Manuscript* with the edited and formatted *Advance Article* as soon as it is available.

You can find more information about *Accepted Manuscripts* in the [Information for Authors](#).

Please note that technical editing may introduce minor changes to the text and/or graphics, which may alter content. The journal's standard [Terms & Conditions](#) and the [Ethical guidelines](#) still apply. In no event shall the Royal Society of Chemistry be held responsible for any errors or omissions in this *Accepted Manuscript* or any consequences arising from the use of any information it contains.



www.rsc.org/dalton

Effect of tri- and tetravalent metal doping on the electrochemical properties of lanthanum tungstate proton conductors

J.M. Porras-Vázquez¹, L. dos Santos-Gómez¹, D. Marrero-López², P.R. Slater³, N. Masó⁴, A. Magrasó⁴⁻⁵, Enrique R. Losilla^{*1}

¹ Universidad de Málaga, Dpto. de Química Inorgánica, 29071-Málaga, Spain.

² Universidad de Málaga, Dpto. de Física Aplicada I, Laboratorio de Materiales y Superficies (Unidad Asociada al C.S.I.C.), 29071-Málaga, Spain.

³ School of Chemistry, University of Birmingham, Birmingham, B15 2TT, UK.

⁴ Department of Chemistry, Centre for Materials Science and Nanotechnology (SMN), University of Oslo, FERMiO, Gaustadalléen 21, NO-0349 Oslo, Norway

⁵ Institut Catala de Nanociencia i Nanotecnologia (ICN2), Bellaterra, Barcelona 08193, Spain

KEYWORDS: $\text{La}_{28-y}\text{W}_{4+y}\text{O}_{54+\delta}\square_{2-\delta}$, doped-lanthanum tungstate, proton conductor, SOFCs,

Abstract

Rare-earth tungstates ($\text{La}_{28-y}\text{W}_{4+y}\text{O}_{54+\delta}\square_{2-\delta}$) have attracted attention recently because of their relatively high proton-electron conductivity and high stability in a CO_2 environment. Since doping on the tungsten-site may increase the conductivity, a new series of compounds with composition $\text{La}_{5.5}\text{W}_{1-x}\text{M}_x\text{O}_{11.25-\delta}$ ($\text{M} = \text{Al}, \text{Ti}$ and Zr ; $x=0, 0.05$ and 0.10) have been investigated. The crystal structure of these materials has been studied using X-ray and time-of-flight neutron powder diffraction by Rietveld analysis. The concentration of oxygen vacancies for hydration in the structure has been indirectly determined by thermogravimetric analysis, and the total conductivity in several $p\text{O}_2$, $p\text{H}_2\text{O}$ and $p\text{D}_2\text{O}$ atmospheres has been studied by impedance spectroscopy. An increase in the conductivity is observed, ranging from 4.1 mS cm^{-1} for the undoped sample to 9.2 mS cm^{-1} for $\text{La}_{5.5}\text{W}_{0.9}\text{Ti}_{0.1}\text{O}_{11.25-\square}$, in wet N_2 at $800 \text{ }^\circ\text{C}$.

1. Introduction

Solid oxide fuel cells (SOFCs) are one of the most promising electrochemical energy conversion devices, directly transforming the chemical energy contained in the fuel into electricity with low emissions of pollutants and high efficiency. Rare-earth tungstates ($\text{La}_{28-y}\text{W}_{4+y}\text{O}_{54+\delta}\square_{2-\delta}$) can be used as electrolytes in fuel cells due to their relatively high proton conductivity,¹⁻⁷ low grain boundary resistance for ionic transport^{4,8,9} and high chemical stability in CO_2 and H_2S atmospheres.^{10,11} These materials exhibit p-type and n-type electronic conductivity in oxidizing and reducing atmosphere, respectively, above ~ 800 °C.^{4,12} The interaction between water vapour and the intrinsic oxygen vacancies explains the predominant proton conductivity at temperatures lower than ~ 700 °C.⁴

In order to increase the conductivity of lanthanum tungstates, several cation substitutions have been investigated. For instance, the substitution of lanthanum for isovalent cations such as Y^{3+} , Nd^{3+} , Gd^{3+} and Er^{3+} , reduces the conductivity on decreasing the ionic radii^{7,13} or the crystal symmetry with ordering of the oxygen vacancies.^{14,15} Donor doping studies with Zr^{4+} and Ce^{4+} showed a reduction in conductivity, due to a decrease in the oxygen vacancy concentration.² Substitution by alkaline-earth elements unexpectedly also leads to a reduction in conductivity, since these elements should act as acceptor dopants and increase the concentration of oxygen vacancies.^{3,4,16,17} The authors may speculate that this behaviour could be attributed to stronger proton–acceptor association, as in other Ti-doped samples¹⁸, or to the fact that the compositions are metastable.¹⁹ This point requires further work to be clarified.

Regarding doping on the tungsten-site, the partial substitution of W^{6+} by Mo^{6+} , $\text{La}_{28-y}(\text{W}_{1-x}\text{Mo}_x)_{4+y}\text{O}_{54+\delta}$ ($x = 0-1$, $y = 0.923$), increases significantly the ambipolar conductivity, making these materials interesting as mixed electronic–proton conductors.^{20,21} The electronic conductivity is substantially enhanced, without altering significantly the proton conductivity, due to the easier reduction of Mo^{6+} compared to W^{6+} .²² Such enhancement in electronic conductivity negates its use as electrolyte for proton conductor solid oxide fuel cells (PC-SOFCs), but it is suitable for hydrogen gas separation membrane applications. Other substitutions, such as W^{6+} by Nb^{5+} , $\text{La}_{5.4}(\text{W}_{1-x}\text{Nb}_x)\text{O}_{11.1-x/2}$ ($0 \leq x \leq 0.2$), increase the oxygen vacancy concentration and enhance the

ionic conductivity.²³ The highest conductivity value was obtained for $\text{La}_{5.4}\text{W}_{0.8}\text{Nb}_{0.2}\text{O}_{11}$, i.e. 10 mS cm^{-1} at $800 \text{ }^\circ\text{C}$, compared to 4 mS cm^{-1} for the non-substituted material, $\text{La}_{5.4}\text{WO}_{11.1}$. Rhenium doping also leads to an increase in the conductivity, from 3 mS cm^{-1} for $\text{La}_{5.5}\text{WO}_{11.25}$, to 4 mS cm^{-1} for a composition with a 20% Re in the tungsten position, at $800 \text{ }^\circ\text{C}$ in wet H_2 .^{21,24}

The aim of this work is to determine the effect of W-site doping with selected elements in an attempt to increase the number of oxide vacancies and, therefore, increase the ionic conductivity of lanthanum tungstate. We have focused on the effect of the substitution of tungsten by aluminium, titanium and zirconium on the structural, microstructural and electrical properties.

2. Experimental

2.1. Synthesis of the powders

Materials with composition $\text{La}_{5.5}\text{W}_{1-x}\text{M}_x\text{O}_{11.25-8}$ ($\text{M} = \text{Al}^{3+}$, Ti^{4+} and Zr^{4+} ; $x=0, 0.05, 0.10$ and 0.15) were prepared by the freeze-drying precursor method from aqueous solutions and ethylenediaminetetraacetic acid (EDTA) as complexing agent. The $\text{La}/(\text{W}+\text{M})$ ratio was fixed to 5.5 to avoid lanthanum oxide segregation based on an earlier report.⁷ Starting materials used as reagents were: La_2O_3 (99.99%, Aldrich), WO_3 (99.99%, Aldrich), $\text{Al}(\text{NO}_3)_3 \cdot 9\text{H}_2\text{O}$ (98%, Aldrich), $\text{Ti}[\text{OCH}(\text{CH}_3)_2]_4$ (99%, Aldrich) and $\text{ZrO}(\text{NO}_3)_2 \cdot 6\text{H}_2\text{O}$ (99% Aldrich), and EDTA (99.5%, Aldrich). Lanthanum oxide was pre-calcined at $1000 \text{ }^\circ\text{C}$ for 2 h in order to achieve dehydration and decarbonation. Precursor solutions were prepared separately by dissolving titanium isopropoxide in ethanol, metal nitrates in distilled water, La_2O_3 in diluted nitric acid, and WO_3 in diluted ammonia. An EDTA solution was added as a complexing agent in a 1:1 ligand:metal molar ratio. The different cation solutions were mixed in stoichiometric relations and the pH was adjusted to 8 by ammonia addition. The volume and cation concentration of the resulting solutions were 125 mL and $\sim 0.1 \text{ M}$ of La^{3+} respectively. The solutions were dropped and frozen in liquid nitrogen, and then dehydrated by vacuum sublimation in a Telstar Cryodos freeze-dryer for 2 days. The amorphous precursor powders were immediately calcined at $300 \text{ }^\circ\text{C}$ to prevent rehydration and then at $800 \text{ }^\circ\text{C}$ for 1 h to remove the residual organic species and achieve crystallization.

These powders were pressed into pellets and fired at 1600 °C for 1 hour. After that the pellets were ground and further characterized by different methods. For simplicity, the $\text{La}_{5.5}\text{W}_{1-x}\text{M}_x\text{O}_{12-\delta}$ samples are hereafter labelled as M_x , where $\text{M} = \text{Al}, \text{Ti}$ and Zr and x is the dopant content.

2.2. Structural and thermal characterization

All compounds were characterized by laboratory X-ray powder diffraction (XRPD) at room temperature. The patterns were collected on a PANalytical X'Pert Pro MPD diffractometer equipped with a Ge(111) primary monochromator and the X'Celerator detector. The overall measurement time was approximately 4 h per pattern over the 10 to 120° (2 θ) angular range, with 0.017° step size.

Time of flight neutron powder diffraction (TOF-NPD) data were recorded on the high resolution diffractometer HRPD at the ISIS pulsed spallation source (Rutherford Appleton Laboratory, UK). 7.5 g of powdered selected samples were loaded into 8 mm diameter vanadium cans and data collected at ambient temperature. The overall measurement time was approximately ~2 hours. All structural analyses were performed using the GSAS suite of programs.²⁵

Thermogravimetric analysis (TGA) data were recorded on a SDT-Q600 analyser (TA Instruments) at a cooling rate of 5 °C·min⁻¹ under wet (~2% H₂O) air.

2.3. Sintering conditions, microstructural and electrical characterization

Dense ceramic pellets (~98% of relative density) were obtained by pressing the powders into disks of 10 mm of diameter and ~1 mm of thickness at 100 MPa, followed by sintering at 1600 °C for 1 hour.

The microstructure of the ceramics was observed by scanning electron microscopy (SEM) (Jeol JSM-6490LV) combined with energy dispersive spectroscopy (EDS) (Oxford Instruments). The grain size of the sintered pellets was estimated from SEM micrographs, using the linear intercept method from at least 30 random lines and three different micrographs with the help of image-analysis software.²⁶

Platinum electrodes were made by coating the pellet surfaces with platinum ink (METALOR® 6082) and gradually heating to 800 °C for 15 min in air to dry and sinter

the electrode. Impedance spectra were acquired using a frequency response analyzer Solartron 1260 in dry (directly from the gas bottle) and wet (bubbling through H₂O) gases (N₂ and 5%H₂-Ar) in the 0.1 Hz to 1 MHz frequency range with an ac perturbation of 100 mV. The spectra were recorded on cooling from 900 to 150 °C with a stabilization time of 15 min between consecutive measurements. The resistance and capacitance values of the different processes were obtained by fitting the impedance spectra data with equivalent circuits using the ZView program.²⁷

The dependence of the conductivity with oxygen partial pressure was measured from O₂ to H₂ at constant p_{H₂O} (~2.5 % H₂O) in a ProboStat measurement cell (NorECs, Norway) by the 2-point 4-wire method. The variation of the conductivity with water partial pressure was performed from dry (bubbling through P₂O₅; p_{H₂O} ~30 ppm) to wet (bubbling through a KBr saturated H₂O solution; p_{H₂O} ~2.5 % H₂O) conditions in O₂. The conductivity was monitored versus time at each new set of conditions to ensure that equilibrium was achieved before taking a measurement.

3. Results and discussion

3.1. Phase existence and structure

XRPD patterns for La_{5.5}W_{1-x}M_xO_{11.25-δ} series were analyzed by the Rietveld method using the structural description reported by Scherb *et al.*²⁸ in the **Fm $\bar{3}$ m** space group. The usual parameters such as histogram scale factors, background and peak shape coefficients were fitted. Due to the presence of heavy cations with large scattering factors compared to oxygen, the refinements of the occupation factors could not be carried out without strong correlations. Therefore, the cation and oxygen contents were fixed to the nominal stoichiometry, where Al³⁺, Ti⁴⁺ and Zr⁴⁺ are replacing W⁶⁺ on the La₂/W₂ site, giving rise to the following structural formulae: La_{14.0}(La_{23.077}W_{20.923-4.923x}M_{4.923x})W₁₄O_{55.3845-7.3845x}□_{0.6135+7.3845x} for M= Al, and La_{14.0}(La_{23.077}W_{20.923-4.923x}M_{4.923x})W₁₄O_{55.3845-4.923x}□_{0.6135+4.923x}, for M= Ti and Zr, which justifies the overall La/W+M ratio of 5.5. Thermal parameters for all atoms were refined isotropically when possible. For different atoms located on the same crystallographic site, their corresponding isotropic thermal factors were constrained to be equal. Selected results of the Rietveld refinements are shown in Table 1. The Rietveld disagreement values were acceptable considering the high degree of atomic disorder of the thermal parameters for

La₂/W₂ and O. This disorder in the cation and anion sublattice has been explained in detail in later studies of the local structure of lanthanum tungstate.^{28, 29}

Figure 1 shows an example of fitting results of XRPD patterns for M_{0.1} (M=Al, Ti and Zr). All remaining samples showed similar fits.

For the aluminium series, the main phase was the lanthanum tungstate-type structure with a minor secondary phase, identified as LaAlO₃ (PDF No 00-031-0022), whose intensity increased on doping (Fig. S1). Since the ionic radius of Al³⁺ in an octahedral environment (0.535 Å) is smaller than that of W⁶⁺ (0.60 Å), it is expected that cell parameters slightly decreased upon Al-substitution. However, the cell parameters surprisingly increased and can be ascribed to a partial minor reduction of W⁶⁺ to W⁵⁺, since a progressive darkening of the samples on increasing Al-content was observed. The diffuse reflectance UV/Vis spectra show a band centred at 453 nm and a broad absorption in the visible region, which is attributed to the d-d transition of W⁵⁺.³⁰ For Al_{0.10}, the decrease in the cell volumes may be due to the fact that Al is not being fully incorporated into the structure and, preferentially segregated to the LaAlO₃ phase, reducing the lanthanum content in LWO phase and consequently its cell volume.

No secondary phases were observed in the case of tetravalent metals up to x=0.10. Dopant content beyond that level, x=0.15, led to the segregation of a significant amount of secondary phases, La₅Ti₅O₁₅ (PDF No 00-048-0480) and La₂Zr₂O₇/ZrO₂ (PDF No 01-073-0444/00-049-1642), for Ti and Zr series, respectively. Therefore, those samples were not further characterised (Fig. S1).

The cell parameters for Ti-doped samples increased with doping (see Table 1). This behaviour was expected, as the ionic radius of titanium 0.605 Å (sixfold coordination) is slightly larger than that of tungsten (0.60 Å). An expansion of the cell volume for Zr_{0.05} was also observed for analogous reason (r[Zr⁴⁺]=0.72 Å). However, for x=0.10 a significant decrease in the cell parameters occurred. Shimura *et al.*² previously reported a contraction of the cell in La_{6-x}Zr_xWO_{12-δ} series.

In order to analyse the role of the dopant, time-of-flight neutron powder diffraction (TOF-NPD) data were collected for La_{5.5}W_{1-x}M_xO_{11.25-x} (M= Ti and Zr; x= 0.05 and 0.10). Refinements were carried out in the Fm $\bar{3}$ m space group and the usual overall parameters, such as histogram scale factors, background and peak shape coefficients were fitted. Atomic positions and anisotropic displacement parameters were

refined as well. Occupation factors were accordingly modified for La2, W2, M and O to reflect two different substitution possibilities, at W2 or La2 site. Rietveld disagreement factors showed a significant improvement when M is substituting onto the W2 positions instead of La2. For instance, R_F values for banks 1/2 dropped from 8.17/5.39 to 7.82/5.24 % when Zr is located at W2 positions, for $Zr_{0.05}$. Similar results were obtained for the remaining samples. These results clearly indicate that the preferred dopant substitution site was W2. An example of the final TOF-NPD Rietveld plots for $Zr_{0.05}$ (replacing W2) is shown in Figure 2. Atomic positions, isotropic atomic displacement parameters, occupancy factors and Rietveld disagreement values are given in Table 2. Anisotropic atomic displacement parameters are given in Table S1.

In addition, occupancy factors were refined for W2 and M. For both Ti-doped samples and $Zr_{0.05}$, Rietveld analyses showed dopant occupancy factors contents very close to the theoretical values; however, for $Zr_{0.10}$, its occupancy factor decreased significantly, to an experimental value of $x \sim 0.02$, indicating that for that sample Zr incorporation was much lower than expected, and the solubility limit for Zr in LWO-based samples is between 0.05 and 0.10. Bearing in mind the XRPD pattern for $Zr_{0.15}$, the evolution in the cell parameters for that series comes from a segregation of $La_2Zr_2O_7/ZrO_2$ not seen in the XRPD pattern (very likely as an amorphous phase) that decreases the cell volume.

3.2. Thermal analysis

The water uptake was monitored by thermogravimetric analysis as a function of temperature to indirectly determine the concentration of oxygen vacancies available in the structure for hydration and, therefore, evaluate the possible differences upon dopant content. The thermogravimetric curves, collected under humidified air, were reproducible on both cooling and heating cycles. Only the curves taken on cooling are compared for the different compositions in Figure 3.

The curves showed the typical behaviour of a proton conducting material with a weight increase upon cooling due to water uptake and the formation of protonic defects, according to the exothermic hydration of oxygen vacancies (Eq. 1).



As expected, the water uptake started approximately at 700 °C, in agreement with the general behaviour of lanthanum tungstates, which are predominantly oxide ion conductors at temperatures above ~800 °C, and predominantly protonic conductors at temperatures lower than ~600 °C.^{3,19} In the insets of the figures, the relationship between the dopant content and the water uptake is represented. For Al-doped samples the water uptake increased with the Al-content, from 0.096 for $M_{0,0}$ to 0.154 moles(H_2O)/moles(LWO) for $Al_{0,05}$, due to a larger concentration of oxygen vacancies in the oxygen sublattice. These results suggest that, despite the minor $LaAlO_3$ segregation, a little amount of Al^{3+} is partially incorporated in the lanthanum tungstate. However, on further increasing x , a decrease in the water content occurred, i.e. 0.142 moles(H_2O)/moles(LWO) for $x = 0.10$, indicating that Al is not being fully incorporated into the structure, and rather is preferentially segregated to the $LaAlO_3$ phase.

For Ti-doping, the water content increased with x from 0.096 to 0.154 moles(H_2O)/moles(LWO) for $x = 0$ and $x = 0.10$, respectively, in agreement with an increase of oxygen vacancies and, consequently, water uptake on doping. This behaviour can be considered as a proof of the success in acceptor doping of lanthanum tungstate. For the Zr-doped samples, the evolution of water uptake versus the dopant content reached a maximum for $x = 0.05$, i.e. 0.137 moles(H_2O)/moles(LWO). However, the increase of Zr content above $x > 0.05$ led to a decrease in the number of water molecules per mole of tungstate, i.e. 0.094 moles(H_2O)/moles(LWO) for $Zr_{0,10}$, due to Zr not fully incorporating into the structure, as TOF-NPD data analysis previously indicated.

3.3. Microstructure and electrical characterization

The sintering procedure used to prepare the ceramic pellets led to very dense specimens with relative density above 98%. The SEM images clearly showed the high density microstructure of the samples (Figure 4). Weight loss due to cation evaporation was not detected after sintering. No indications of liquid phase formation or phase segregations at the grain boundary were found.

Particle size analyses show a average grain size around 24 μm for the undoped sample, and 21, 23, 19, 21 and 20 μm for $Al_{0,05}$, $Ti_{0,05}$, $Ti_{0,10}$, $Zr_{0,05}$ and $Zr_{0,10}$, respectively. By considering that the grain size is similar for all the samples, these

dopants have not significant effects on the grain growth and densification of the ceramics.

EDS mappings showed that all samples were chemically homogenous in La and W. Dopants could not be detected without significant errors due to their low concentrations. Figures S3, S4 and S5 display the element mapping results obtained on the surface of $\text{Al}_{0.05}$, $\text{Ti}_{0.10}$ and $\text{Zr}_{0.10}$, respectively. These samples showed a homogeneous distribution of W and La without evidence of phase segregations.

All the samples were studied by impedance spectroscopy in different atmospheres, dry and wet N_2 and wet 5% H_2 -Ar. Figure 5 shows representative impedance spectra at 250 °C in wet N_2 for $\text{La}_{5.5}\text{W}_{0.95}\text{M}_{0.05}\text{O}_{11.25-\delta}$ (M= Al, Ti and Zr) samples. All spectra showed similar shapes with two contributions attributed to grain interior (bulk) and electrode processes. The grain boundary contribution was not observed for any of the samples, likely due to the large grain size ($> 10 \mu\text{m}$). A similar behaviour was observed for all compositions. The spectra were simulated by using the following equivalent circuit: $(R_b Q_b) Q_e$, where the subscripts b and e denote grain interior and electrode processes, respectively. The capacitance values of each contribution were in the typically expected range of $\sim \text{pF} \cdot \text{cm}^{-1}$ for the bulk, and $\text{mF} \cdot \text{cm}^{-1}$ for the electrode response.

The Arrhenius plots in wet N_2 for the $\text{La}_{5.5}\text{W}_{1-x}\text{M}_x\text{O}_{11.25-\delta}$ (M= Al, Ti, and Zr) series, taken under isobaric conditions, are shown in Figure 6, whereas isothermal overall conductivity values at 800 °C versus the dopant content in the three atmospheres are displayed in Figure 7 and Table S2. The conductivities for all compositions were higher in a wet atmosphere, indicating the presence of proton conductivity. Above 800 °C the values of conductivity were nearly independent of the water content, suggesting that oxide ions were the main charge carrier in that region.

Regarding the behaviour of the samples on doping, all compositions showed an increase in conductivity with respect to the parent compound, indicating an acceptor-doping effect. For instance, at 800 °C, conductivity increases from 4.1 mS cm^{-1} for M_0 to 9.2 and 9.9 mS cm^{-1} for $\text{Ti}_{0.10}$ and $\text{Al}_{0.05}$, respectively. At 500 °C, from 0.9 for M_0 to 1.4 and 1.8 mS cm^{-1} for $\text{Ti}_{0.10}$ and $\text{Al}_{0.05}$, respectively (all values given for measurements in a wet N_2 atmosphere). However, the lower conductivity values for $\text{Al}_{0.10}$ and $\text{Zr}_{0.10}$ are

ascribed to the saturation limit of the dopant in LWO and, the consequent segregation of secondary phases.

The dependence of the conductivity versus oxygen partial pressure for $\text{Al}_{0.05}$ and $\text{Ti}_{0.10}$ is shown in Figure 8, along with the same measurements for undoped lanthanum tungstate (LWO54, lines) from ref [31]. The plots showed some common trends, with the overall behaviour typical of a mixed ionic-electronic conductor as reported earlier.^{6,9} The conductivity was essentially independent of the $p\text{O}_2$ at intermediate pressures, indicating dominating ionic conductivity. At high temperatures and high $p\text{O}_2$, the conductivity increased with increasing the $p\text{O}_2$, indicating the presence of p-type electronic conductivity. At high temperatures and low $p\text{O}_2$, the conductivity increased with decreasing the $p\text{O}_2$, which is consistent with n-type conductivity.

$\text{Ti}_{0.10}$ and $\text{Al}_{0.05}$ show higher conductivities than $\text{M}_{0.0}$ in the whole $p\text{O}_2$ range.³¹ The differences in conductivity in the samples are mainly ascribed to variations in the ionic conductivity. The impact on the electronic conductivity, although significant, is relatively minor.

It is worth mentioning that the stability of $\text{Ti}_{0.10}$ and $\text{Al}_{0.05}$ under reducing conditions at high temperatures (>1000 °C) is low, and the measurements after such a heat treatment became unstable and non reproducible. This overall behaviour is likely related to the increase in oxygen vacancy concentration (effective acceptor dopants) and may be ascribed to the fact that LWO does not tolerate large variations of the “ideal” oxygen vacancy concentration of 0.5 vacancies per formula unit ($\text{La}_{28-y}\text{W}_{4+y}\text{O}_{54+\delta}\square_{2-\delta}$ $y=1$, the LWO54 composition).¹⁹

The variation of the conductivity with $p\text{H}_2\text{O}$ (see Figure 9) showed the behaviour of a typical proton conductor, in accordance with the conductivity characteristics of LWO.¹⁹ The conductivity decreased on decreasing $p\text{H}_2\text{O}$, and the slope was the steepest at the lowest temperatures ($\sim 1/4$ for $\text{Al}_{0.05}$ and approaching $1/3$ for $\text{Ti}_{0.10}$ at 500 °C), as expected for a typical proton conductor. The flattening of the conductivity at low $p\text{H}_2\text{O}$ and high temperatures indicated that oxide ion conductivity became more dominating, as commented earlier. This is expected since the material dehydrates upon increasing temperature due to the exothermic nature of the hydration reaction (Eq. 1).

Complementary measurements were performed in order to confirm the role of protons in the materials tested here. First, temperature ramps (isobaric measurements) were performed in wet and dry O₂ (Figure S6) for Al_{0.05} and Ti_{0.10}. These confirm the strong impact of water content on the conductivity shown in Figure 9. More importantly, the isotope effect on the conductivity when changing from H₂O-O₂ to D₂O-O₂ (Figure S7) confirmed the presence of dominating proton conductivity at low temperatures.

Conclusions

La_{5.5}W_{1-x}M_xO_{11.25-δ} (M= Al, Ti and Zr; x=0, 0.05 and 0.10) were prepared by the freeze-drying precursor method. XRPD analysis showed that no secondary phases were observed for tetravalent metal dopants. The cell parameters for Ti-doped and Zr_{0.05} samples increased with doping as expected, however, a decrease in the cell volume took place for Zr_{0.1}. TOF-NPD analysis confirmed the introduction of the dopant in the W2 position, although it also indicated that for Zr_{0.10}, the dopant was not fully incorporated. Water uptake was followed by thermogravimetry. The curves showed the typical behaviour of proton conducting materials. All the samples were measured by impedance spectroscopy under dry and wet N₂ and wet 5% H₂-Ar. In all cases, the conductivities were higher in a wet atmosphere, indicating the presence of proton conductivity. Furthermore, the conductivity increased on Ti doping due to a higher concentration of ionic charge carriers, in agreement with the evolution of the cell parameters on doping and the TGA results. The variation of the conductivity with water vapour partial pressure and the isotope effect confirmed the presence of proton conductivity in these samples.

Acknowledgments

This work was supported by MINECO through the MAT2013-41836-R research grant (Spain) which is co-funded by FEDER. J.M.P.V. thanks Andalucía Tech, and A.M. and N.M. thank the Research Council of Norway (Grant 219731) for the funding. L.dS.G. thanks to the Spanish Ministry of Education, Culture and Sports for her FPU studentship. We would like to express thanks to the ISIS neutron diffraction facility at

the Rutherford Appleton Laboratory for the provision of beam time for the neutron diffraction experiments, and to Kevin Knight for help with the collection of these data.

References

- [1] M. Yoshimura and J. F. Baumard, *Mater. Res. Bull.*, 1975, **10**, 983-988.
- [2] T. Shimura, S. Fujimoto and H. Iwahara, *Solid State Ionics*, 2001, **143**, 117-123.
- [3] R. Haugrud, *Solid State Ionics*, 2007, **178**, 555.
- [4] R. Haugrud and K. Kjølseth, *J. Phys. Chem. Solids*, 2008, **69**, 1758-1765.
- [5] S. Escolástico, V. B. Vert and J. M. Serra, *Chem. Mater.*, 2009, **21**, 3079-3089.
- [6] R. Haugrud, H. Fjeld, K. R. Haug and T. Norby, *J. Electrochem. Soc.*, 2007, **154**, B77-B81.
- [7] A. Magrasó, C. Frontera, D. Marrero-López and P. Núñez, *Dalton Trans.*, 2009, 10273-10283.
- [8] C. Solis, S. Escolastico, R. Haugrud and J. M. Serra, *J. Phys. Chem. C*, 2011, **115**, 11124.
- [9] A. Magrasó, J. M. Polfus, C. Frontera, J. Canales-Vazquez, L. Kalland, C. H. Hervoches, S. Erdal, R. Hancke, S. S. Islam, T. Norby and R. Haugrud, *J. Mater. Chem.*, 2012, **22**, 1762-1764.
- [10] J. M. Serra, S. Escolastico, M. Balaguer, W. A. Meulenberg, H. P. Buchkremer, T. Scherb, G. Schumacher, M. W. Lumey and R. Dronskowski, Proceedings of 2009 E-MRS Fall Meeting, September 14–18, Warsaw, 2009, p. 140.
- [11] S. Escolastico, C. Solis and J. M. Serra, *Int. J. Hydrogen Energy*, 2011, **36**, 11946-11954.
- [12] K. V. Kravchyk, E. Quarez, C. Solis, J. M. Serra and O. Joubert, *Int. J. Hydrogen Energy*, 2011, **36**, 13059-13066.
- [13] S. Escolastico, C. Solis and J. M. Serra, *Solid State Ionics*, 2012, **216**, 31-35.
- [14] A. Lashtabeg, J. Bradley, A. Dicks, G. Auchterlonie and J. Drennan, *J. Solid State Chem.*, 2010, **183**, 1095-1101.

- [15] N. Diot, P. Benard-Rocherulle and R. Marchand, *Powder Diffr.*, 2000, **15**, 220-226.
- [16] A. Magraso, C. H. Hervoche, I. Ahmed, S. Hull, J. Nordstrom, A. W. B. Skilbred and R. Haugrud, *J. Mater. Chem. A*, 2013, **1**, 3774-3782.
- [17] M. J. Zayas-Rey, L. dos Santos-Gómez, A. Cabeza, D. Marrero-López and E. R. Losilla, *Dalton Trans.* 2014, **43**, 6490-6499.
- [18] M. Huse, T. Norby and R. Haugrud, *Int. J. Hydrogen Energy* 2012, **37**, 8004-16.
- [19] A. Magrasó and R. Haugrud, *J. Mater. Chem A*, 2014, **2.32**: 12630-12641.
- [20] M. Amsif, A. Magrasó, D. Marrero-López, J. C. Ruíz-Morales, J. Canales-Vázquez and P. Nuñez, *Chem. Mater.* 2012, **24**, 3868-3877.
- [21] J. Seeger, M. E. Ivanova, W. A. Meulenberg, D. Sebold, D. Stöver, T. Scherb, G. Schumacher, S. Escolástico, C. Solís and J. M. Serra, *Inorg. Chem.* 2013, **52**, 10375-10386.
- [22] A. Magrasó, *Journal of Power Sources*, 2013, **240**, 583-588.
- [23] M. J. Zayas-Rey, L. dos Santos-Gómez, D. Marrero-López, L. León-Reina, J. Canales-Vázquez, M. A. G. Aranda and E. R. Losilla, *Chem. Mater.* 2013, **25**, 448-456.
- [24] S. Escolastico, J. Seeger, S. Roitsch, M. Ivanova, W. A. Meulenberg and J. Serra, *ChemSusChem*, 2013, **6**, 1523-1532.
- [25] A. C. Larson and R. B. V. Dreele, General Structure Analysis System (GSAS) program. Los Alamos National Lab. Rep. No. LA-UR-86748, 1994.
- [26] Estereologia, Joao Abrantes, 1998, UIDM, ESTG, Polytechnic Institute of Viana do Castelo, Viana do Castelo, Portugal
- [27] D. Johnson, ZView: a Software Program for IES Analysis, Version 2.8, Scribner Associates, Inc. Southern Pines, NC, 2002.
- [28] T. Scherb, S.A.J. Kimber, C. Stephan, P.F. Henry, G. Schumacher, J. Just, S. Escolástico, J.M. Serra, J. Seeger, A.H. Hill, J. Banhart, arXiv preprint arXiv:1305.3385 (2013).

- [29] L-E. Kalland, A. Magrasó, A. Mancini, C. Tealdi, and L. Malavasi. *Chem. Mater.* 2013, **25**, 2378-2384.
- [30] Z. Gu, Y. Ma, T. Zhai, B. Gao, W. Yang, and J. Yao, *Chem. Eur. J.* 2006, **12**, 7717-7723.
- [31] S. Erdal, L-E. Kalland, R. Hancke, J. Polfus, R. Haugsrud, T. Norby and A. Magrasó. *Int. J. Hydrogen Energy* 2012, **37(9)**, 8051-8055.

Figure captions

Figure 1. Rietveld plots [observed data (crosses), calculated pattern (continuous line), and difference curve (bottom)] for: a) $\text{La}_{5.5}\text{W}_{0.90}\text{Al}_{0.1}\text{O}_{11.10}$, b) $\text{La}_{5.5}\text{W}_{0.90}\text{Ti}_{0.1}\text{O}_{11.15}$ and c) $\text{La}_{5.5}\text{W}_{0.90}\text{Zr}_{0.1}\text{O}_{11.15}$ from XRPD data.

Figure 2. Rietveld plots [observed data (crosses), calculated pattern (continuous line), and difference curve (bottom)] for bank 1 (left) and bank 2 (right) for $\text{La}_{5.5}\text{W}_{0.95}\text{Zr}_{0.05}\text{O}_{11.20}$ from TOF-NPD data.

Figure 3. Thermogravimetric curves for: a) $\text{La}_{5.5}\text{W}_{1-x}\text{Al}_x\text{O}_{11.25-1.5x}$, b) $\text{La}_{5.5}\text{W}_{1-x}\text{Ti}_x\text{O}_{11.25-x}$ and c) $\text{La}_{5.5}\text{W}_{1-x}\text{Zr}_x\text{O}_{11.25-x}$ nominal series performed under humidified air from 1000 °C to room temperature on cooling. The inset shows the number of water molecules per mole of lanthanum tungstate from 200 to 800 °C as a function of dopant content.

Figure 4. SEM micrograph of the surface of $\text{La}_{5.5}\text{WO}_{11.25}$, $\text{La}_{5.5}\text{W}_{0.95}\text{Ti}_{0.05}\text{O}_{11.20}$, $\text{La}_{5.5}\text{W}_{0.95}\text{Zr}_{0.05}\text{O}_{11.20}$ and $\text{La}_{5.5}\text{W}_{0.95}\text{Al}_{0.05}\text{O}_{11.10}$ sintered at 1600 °C for 1h.

Figure 5. Representative impedance spectra for $\text{La}_{5.5}\text{W}_{0.95}\text{M}_{0.05}\text{O}_{11.25-\delta}$ (M= Al, Ti and Zr) samples under wet N_2 at 250 °C.

Figure 6. Arrhenius plots of the total conductivity for $\text{La}_{5.5}\text{W}_{1-x}\text{M}_x\text{O}_{11.25-\delta}$ (M= Al, Ti and Zr) series in wet N_2 .

Figure 7. Conductivity plots versus dopant content for $\text{La}_{5.5}\text{W}_{1-x}\text{M}_x\text{O}_{11.25-\delta}$ (M= Al, Ti, and Zr) series in dry and wet N_2 and wet 5% H_2 -Ar at 800 °C.

Figure 8. Variation of the overall conductivity as a function of oxygen partial pressure for $\text{La}_{5.5}\text{W}_{1-x}\text{M}_x\text{O}_{11.25-\delta}$ (M= Al, Ti) at different temperatures compared to the conductivity values of LWO54 (lines) from reference [18]. Water vapour partial pressure was kept constant (~2.5% H_2O).

Figure 9. Variation of the overall conductivity as a function of water vapour partial pressure for $\text{La}_{5.5}\text{W}_{1-x}\text{M}_x\text{O}_{11.25-\delta}$ (M= Al, Ti) at different temperatures. Oxygen partial pressure was kept constant (1 atm O_2).

Table captions

Table 1. Cell parameters, disagreement factors and amount of LaAlO_3 for $\text{La}_{5.5}\text{W}_{1-x}\text{M}_x\text{O}_{11.25-\delta}$ (M= Al, Ti and Zr, x=0, 0.05 and 0.10)

Table 2. Cell parameters, atomic positions, isotropic atomic displacement parameters, occupancy factors and Rietveld agreement factors for $\text{La}_{5.5}\text{W}_{1-x}\text{M}_x\text{O}_{11.25-\delta}$ (M= Ti and Zr, x= 0.05 and 0.10) from TOF-NPD data.

Table 1. Cell parameters, disagreement factors and amount of LaAlO_3 for $\text{La}_{5.5}\text{W}_{1-x}\text{M}_x\text{O}_{11.25-\delta}$ (M= Al, Ti and Zr, x=0, 0.05 and 0.10)

	a (Å)	V (Å³)	R_{wp} (%)	R_F (%)	LaAlO₃ (wt%)
La_{5.5}WO_{11.25}	11.1805(1)	1397.60(3)	8.42	5.10	-
La_{5.5}W_{0.95}Al_{0.05}O_{11.175}	11.1939(1)	1402.62(2)	6.22	5.68	1.8(1)
La_{5.5}W_{0.90}Al_{0.10}O_{11.1}	11.1909(1)	1401.50(2)	5.89	5.38	3.9(1)
La_{5.5}W_{0.95}Ti_{0.05}O_{11.2}	11.1812(1)	1397.85(2)	12.77	7.44	-
La_{5.5}W_{0.90}Ti_{0.10}O_{11.15}	11.1910(1)	1401.54(2)	9.26	4.44	-
La_{5.5}W_{0.95}Zr_{0.05}O_{11.2}	11.1857(1)	1399.54(2)	10.22	5.53	-
La_{5.5}W_{0.90}Zr_{0.10}O_{11.15}	11.1703(1)	1393.77(2)	10.04	5.51	-

Table 2. Cell parameters, atomic positions, isotropic atomic displacement parameters, occupancy factors and Rietveld agreement factors for $\text{La}_{5.5}\text{W}_{1-x}\text{M}_x\text{O}_{11.25-\delta}$ (M= Ti and Zr, x= 0.05 and 0.10) from TOF-NPD data.

	$\text{La}_{5.5}\text{W}_{0.95}\text{Ti}_{0.05}\text{O}_{11.2}$	$\text{La}_{5.5}\text{W}_{0.90}\text{Ti}_{0.10}\text{O}_{11.15}$	$\text{La}_{5.5}\text{W}_{0.95}\text{Zr}_{0.05}\text{O}_{11.2}$	$\text{La}_{5.5}\text{W}_{0.90}\text{Zr}_{0.10}\text{O}_{11.15}$
a (Å)	11.1772(1)	11.1788(1)	11.1832(1)	11.1768(1)
V (Å ³)	1396.37(2)	1396.98(2)	1398.61(2)	1396.21(1)
R_{WP}^{N1}/R_{WP}^{N2} (%)	3.74/2.79	4.84/4.32	3.60/2.47	4.41/3.81
R_P^{N1}/R_P^{N2} (%)	3.43/2.64	4.52/3.89	3.54/2.48	4.10/3.64
R_F^{N1}/R_F^{N2} (%)	8.27/6.39	8.67/6.49	7.82/5.24	8.41/5.88
La(1) , 4b, (½, ½, ½)				
U _{iso} × 100 (Å ²)	0.4(1)	0.5(1)	0.8(1)	0.6(1)
W(1) , 4a, (0, 0, 0)				
U _{iso} × 100 (Å ²)	0.8(1)	1.0(1)	0.3(1)	0.1(1)
La2/W2/M , 48h, (0, y, y)				
y	0.2369(1)	0.2371(1)	0.2364(1)	0.2434(1)
U _{iso} × 100 (Å ²)	0.1(1)	0.2(1)	0.4(1)	0.3(1)
Occupancy factor	0.481(-)/ 0.014(1)/0.006(1)	0.481(-)/ 0.092(1)/0.010(1)	0.481(-)/ 0.014(1)/0.006(1)	0.481(-)/ 0.017(1)/0.002(1)
O(1) , 96k, (x, x, z)				
x	0.1115(1)	0.1118(1)	0.1130(1)	0.1129(1)
z	0.0645(1)	0.0632(1)	0.0659(1)	0.0652(1)
U _{iso} × 100 (Å ²)	2.5(1)	2.2(1)	2.1(1)	2.1(1)
O(2) , 32f, (x, x, x)				
x	0.3660(1)	0.3665(1)	0.3663(1)	0.3672(1)
U _{iso} × 100 (Å ²)	1.0(1)	1.0(1)	1.4(1)	1.3(1)
Occupancy factor	0.973(1)	0.965(1)	0.973(1)	0.977(1)

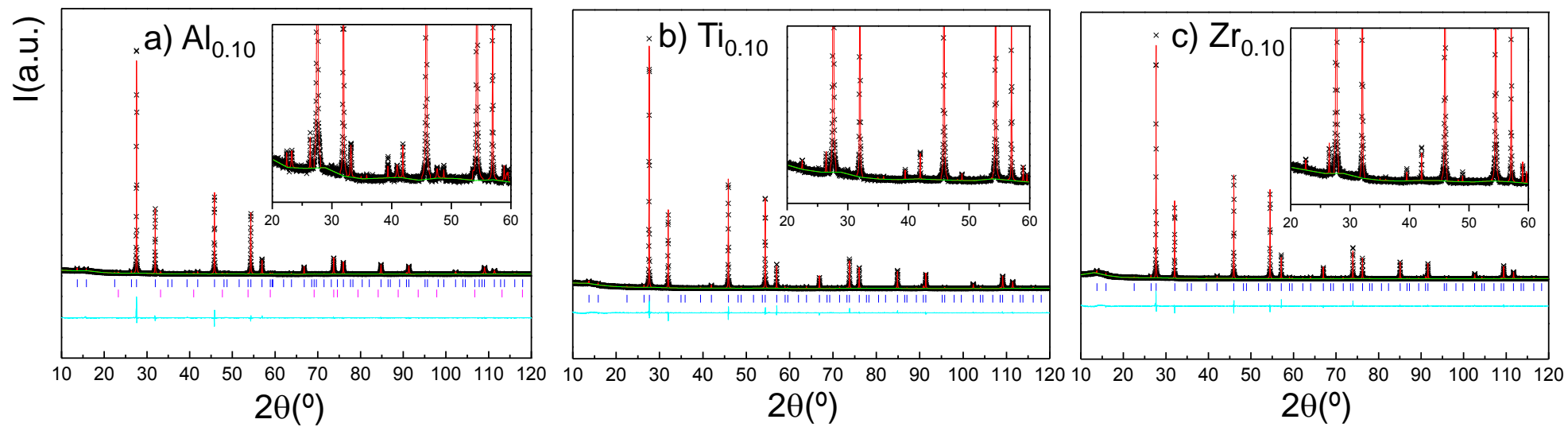
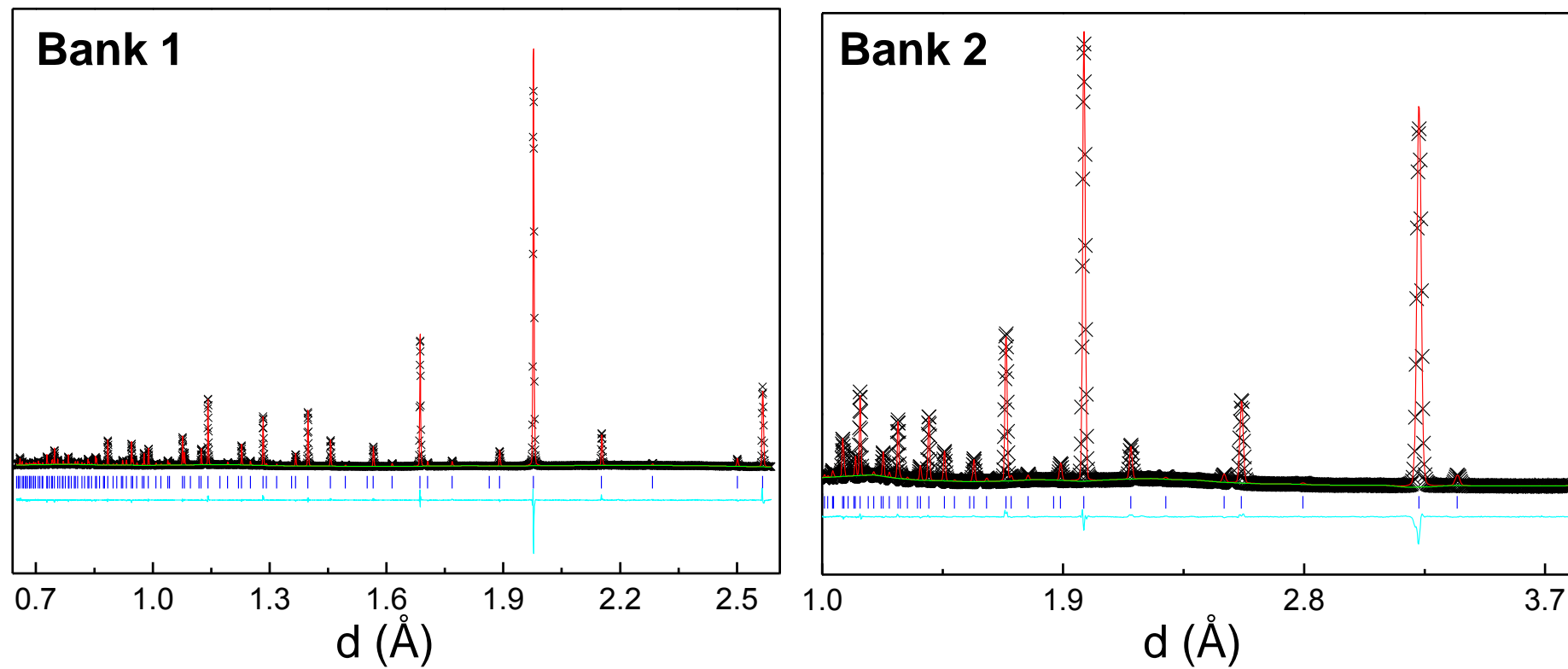


Figure 1

**Figure 2**

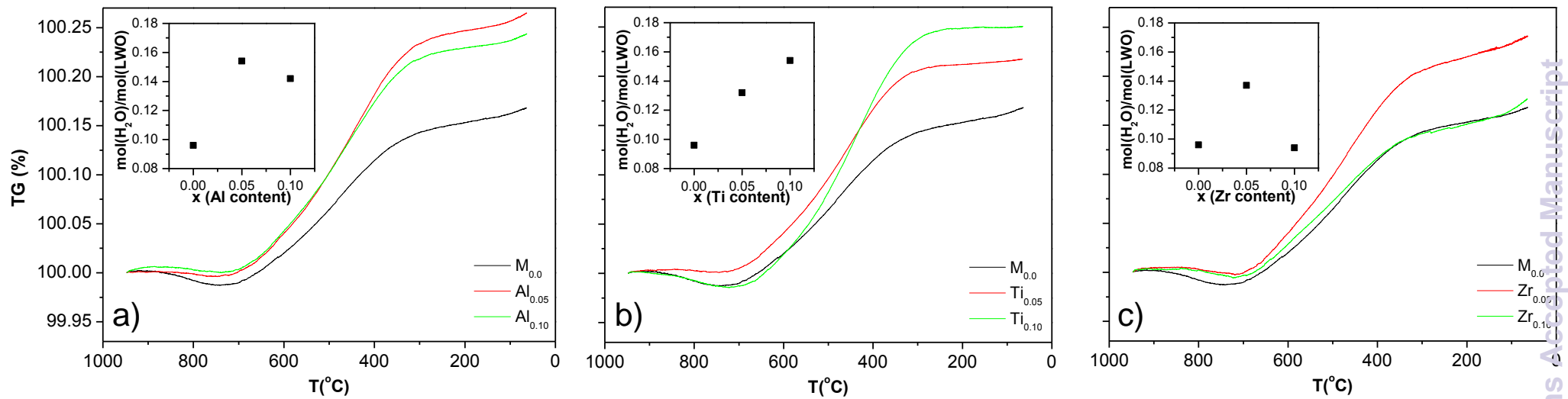
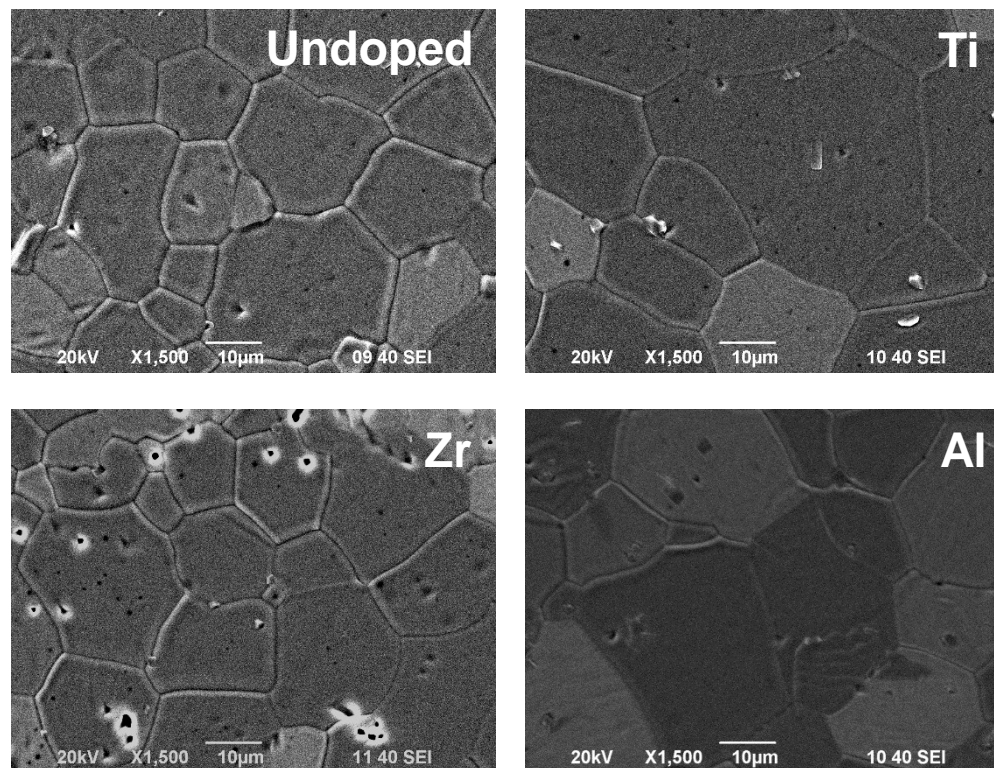


Figure 3

**Figure 4**

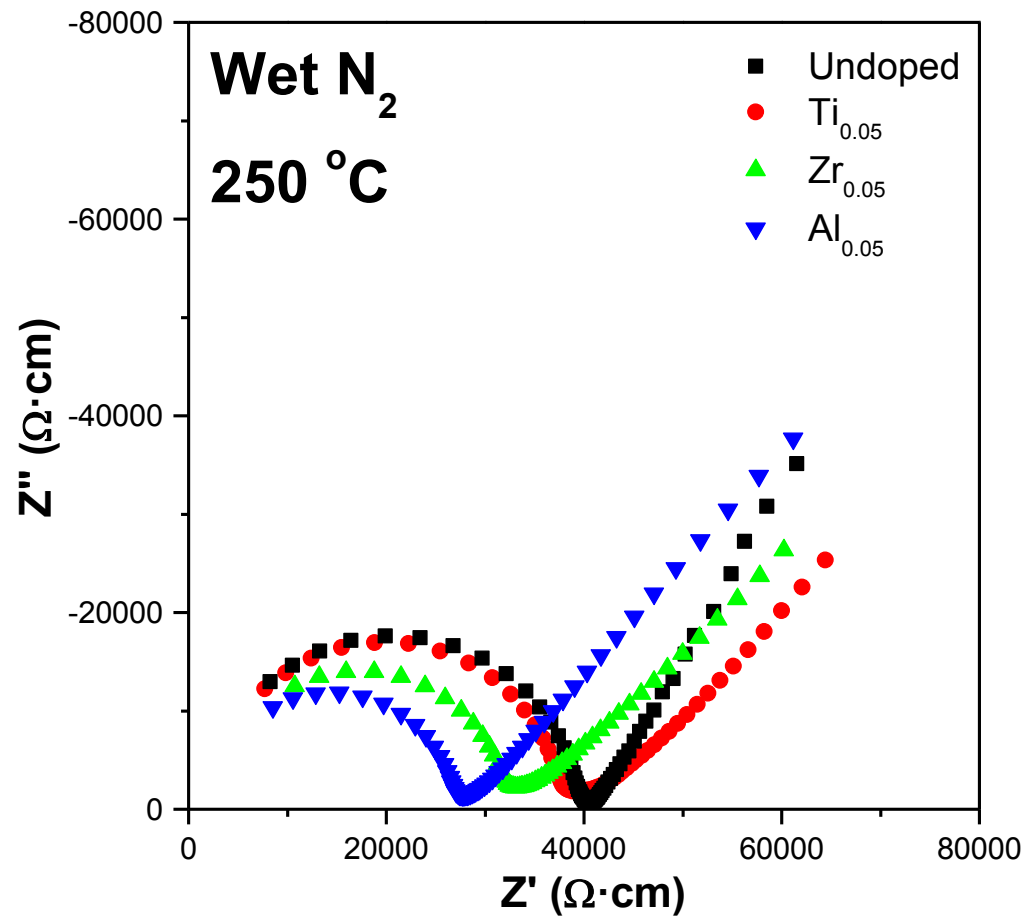


Figure 5

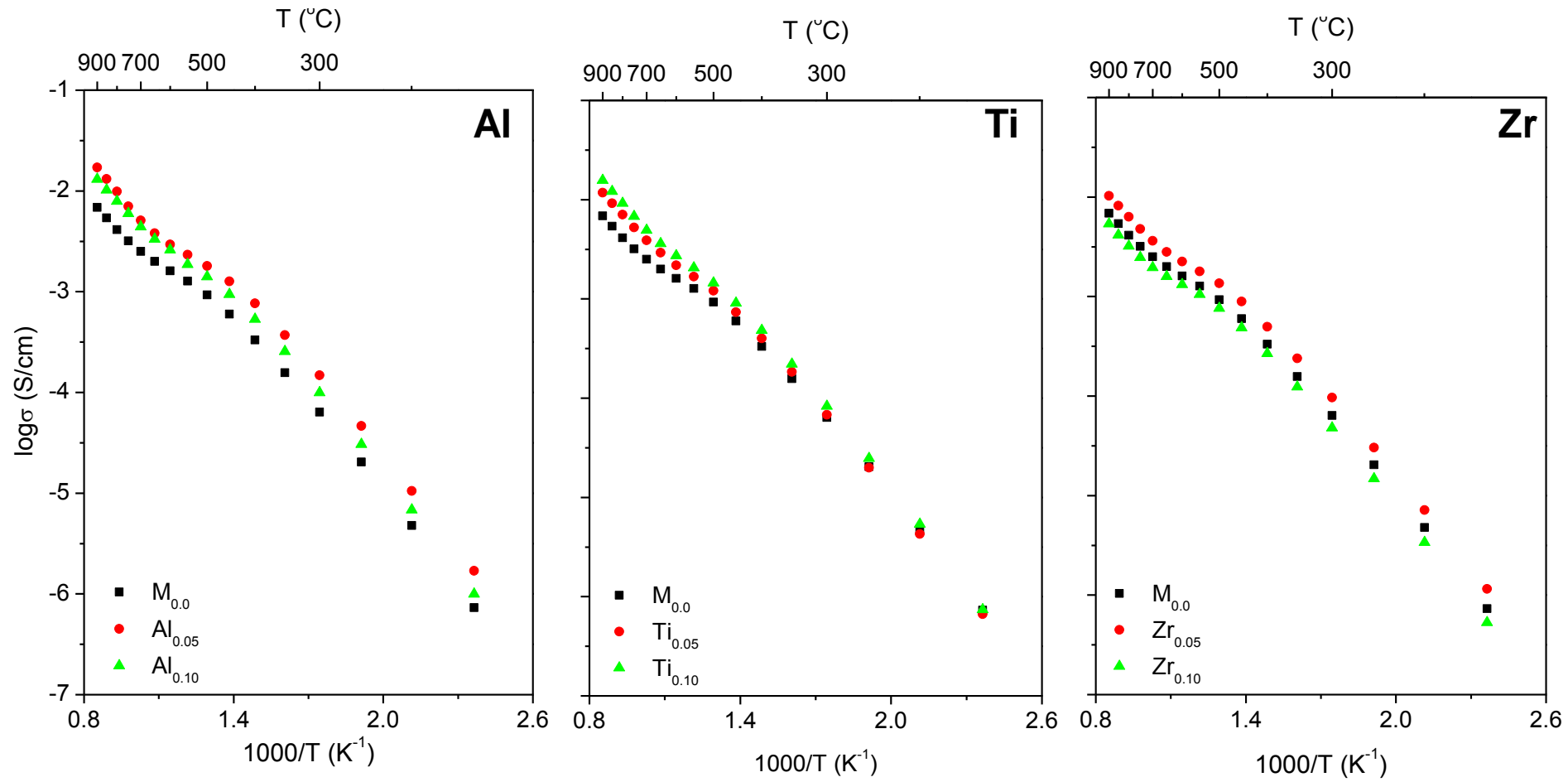


Figure 6

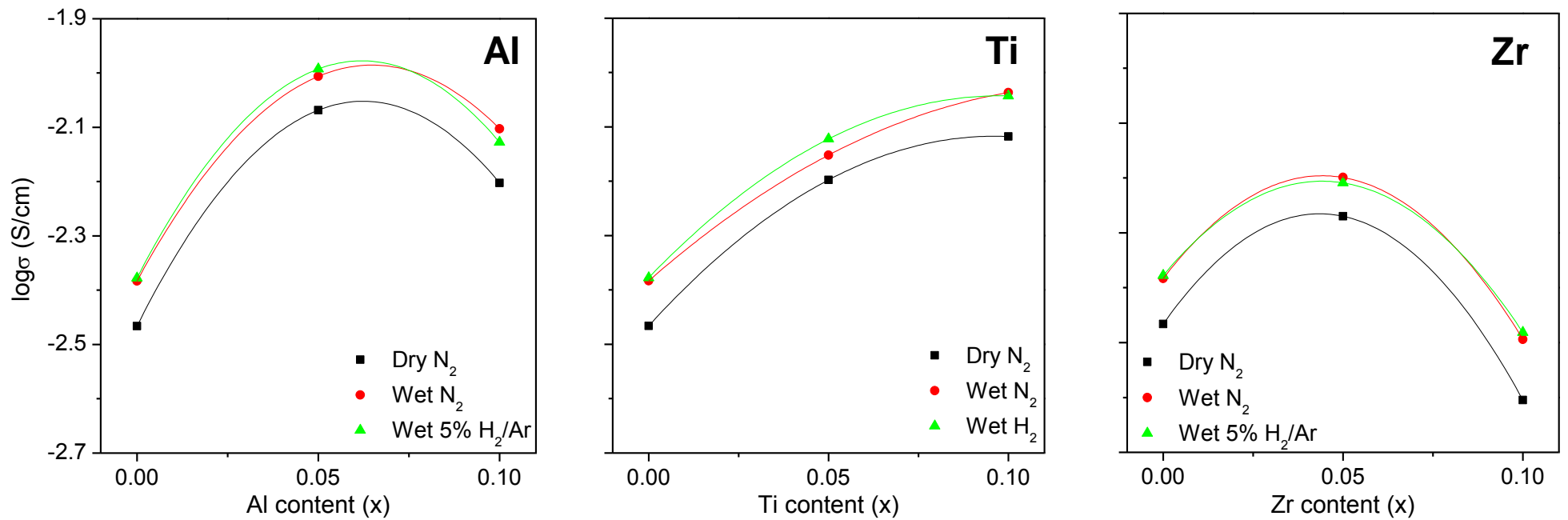


Figure 7

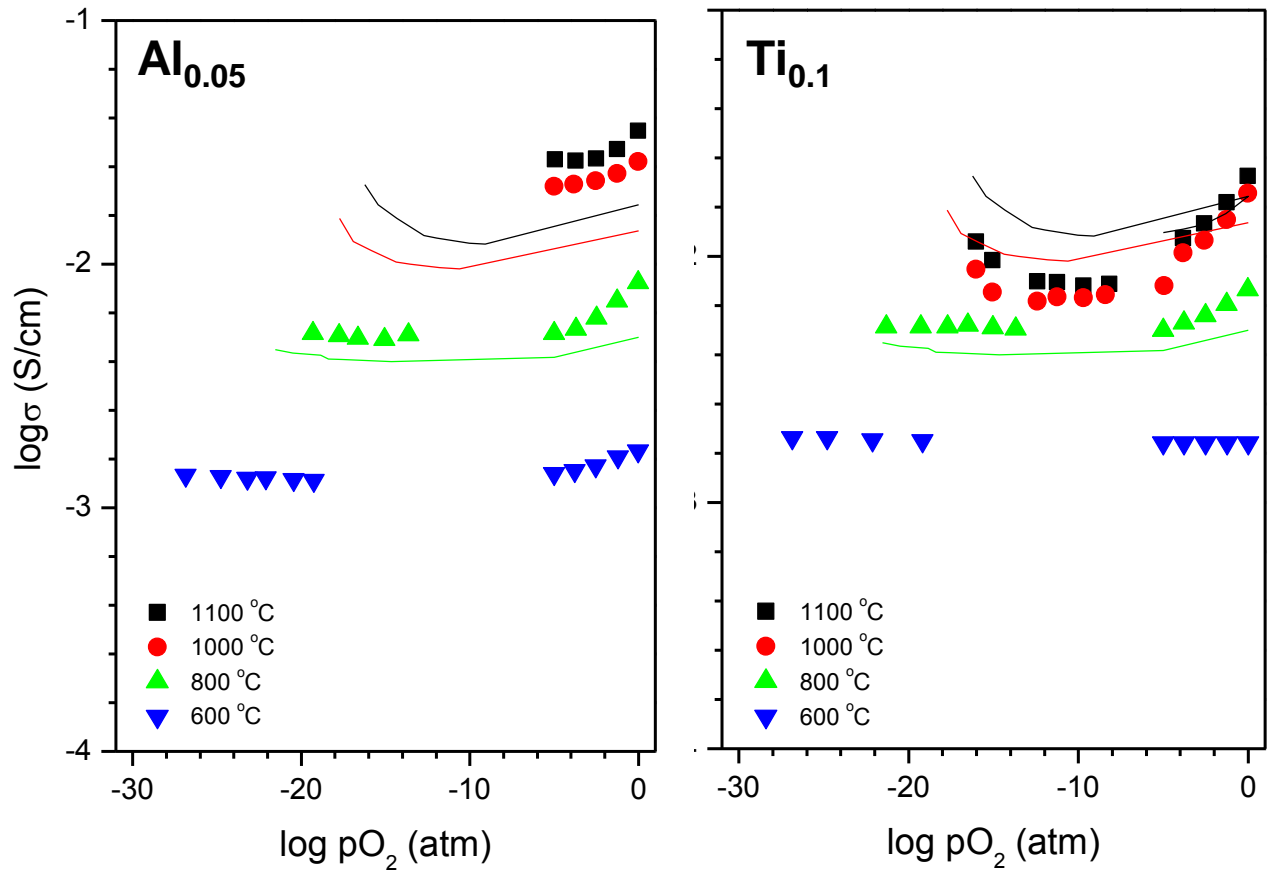


Figure 8

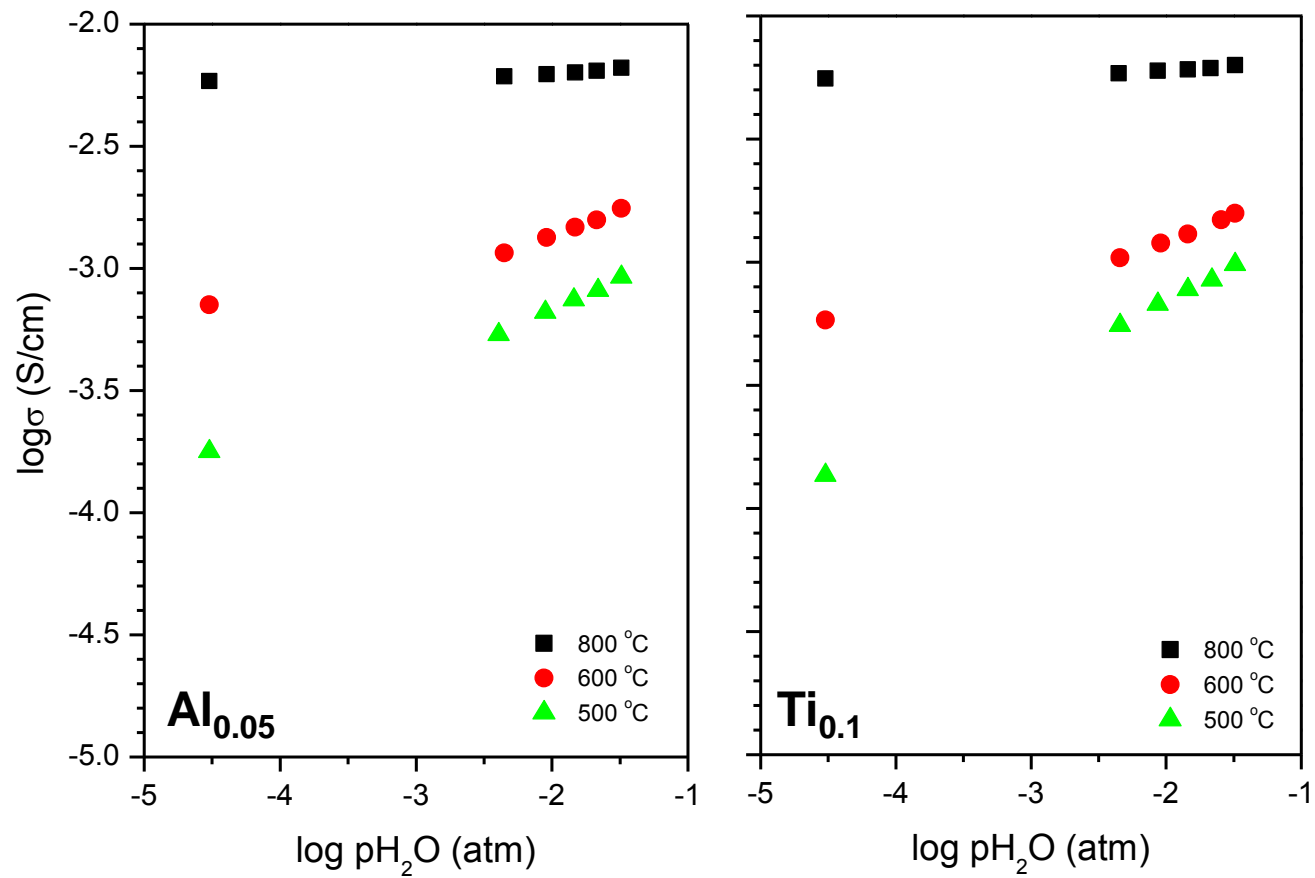
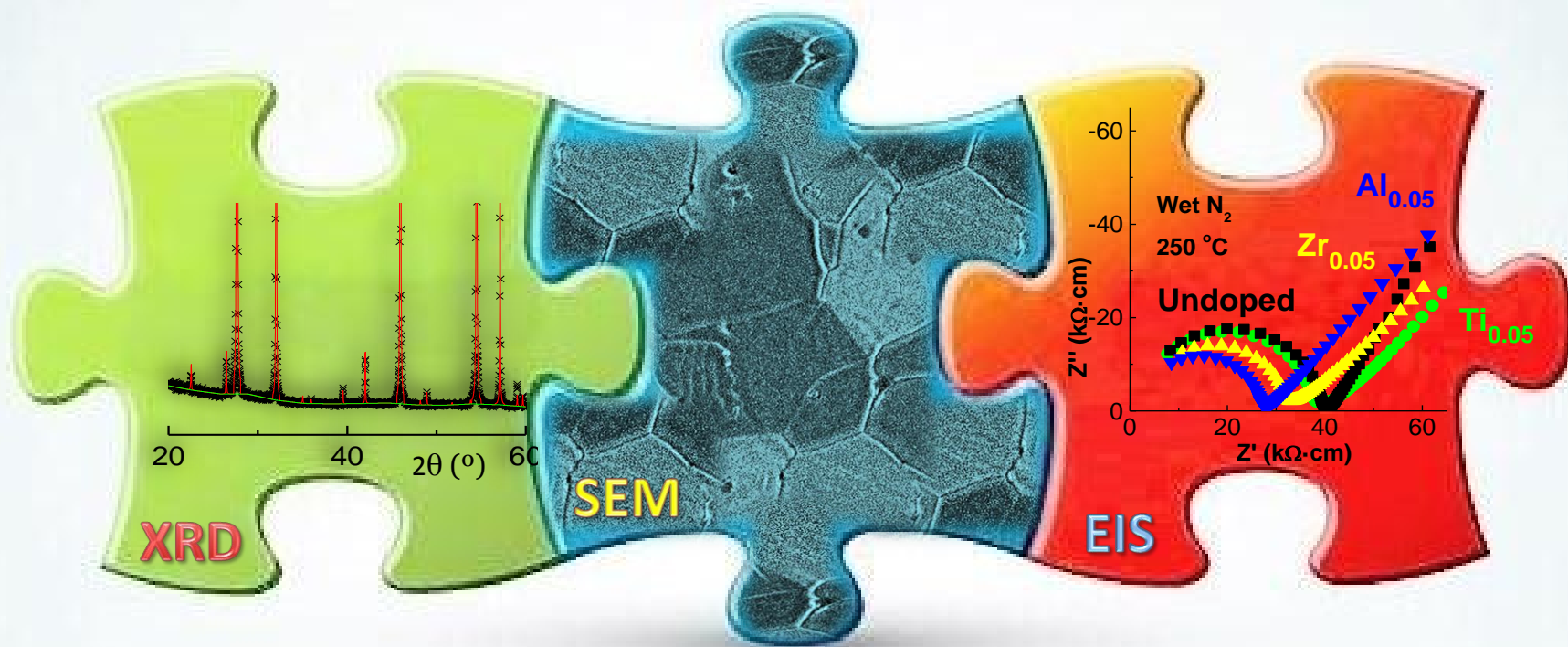


Figure 9



TOC caption

Metal doping on lanthanum tungstates at W2 site was confirmed by TOF-NPD. TGA and EIS demonstrated proton conductivity.